Quasiequilibrium optical nonlinearities from spin-polarized carriers in GaAs

Arjun Joshua* and V. Venkataraman
Department of Physics, Indian Institute of Science, Bangalore, India 560012

(Received 10 July 2007; revised manuscript received 31 October 2007; published 7 February 2008; corrected 8 February 2008)

Semiconductor Bloch equations, which microscopically describe the dynamics of a Coulomb interacting, spin-unpolarized electron-hole plasma, can be solved in two limits: the coherent and the quasiequilibrium regimes. These equations have been recently extended to include the spin degree of freedom and used to explain spin dynamics in the coherent regime. In the quasiequilibrium limit, one solves the Bethe-Salpeter equation in a two-band model to describe how optical absorption is affected by Coulomb interactions within a spin unpolarized plasma of arbitrary density. In this work, we modified the solution of the Bethe-Salpeter equation to include spin polarization and light holes in a three-band model, which allowed us to account for spin-polarized versions of many-body effects in absorption. The calculated absorption reproduced the spin-dependent, density-dependent, and spectral trends observed in bulk GaAs at room temperature, in a recent pump-probe experiment with circularly polarized light. Hence, our results may be useful in the microscopic modeling of density-dependent optical nonlinearities due to spin-polarized carriers in semiconductors.

DOI: 10.1103/PhysRevB.77.085202 PACS number(s): 71.10.−w, 72.25.Fe, 78.20.Ci

I. INTRODUCTION

As the nascent field of spintronics[1] is merged with optoelectronics, it becomes increasingly important to understand the physics of the optical properties of spin-polarized carriers in semiconductors, which are nowadays studied by circularly polarized pump-probe experiments.[2] This degree of freedom of the spin, in the optical properties of photoexcited semiconductors, is mostly ignored in the literature. For spin-unpolarized photoexcited carriers in a pure semiconductor, it is known that the Coulomb attraction between the electron and hole created by a photon causes excitonic resonances and enhances its absorption.[3] As the background electron-hole plasma density is increased, the long-ranged Coulomb interaction between this photoexcited electron-hole pair and the plasma can no longer be neglected. Semiconductor Bloch equations (SBEs) fully describe this interacting plasma and its time-dependent dynamics. SBEs may be solved in two different time scales: the coherent regime (where the induced dipole moment follows the optical field without dephasing) or the quasiequilibrium regime. In many applications, for example, semiconductor laser diodes, it may be assumed that the electrons and holes are thermalized within their respective bands.[4] This quasiequilibrium approximation simplifies the original coupled SBEs. The resulting microscopic theory for the effect of a spin-unpolarized interacting plasma (arbitrary density) on absorption agrees well with experiment.[5] Here, the linear optical susceptibility is obtained by solving the Bethe-Salpeter equation in the (quasistatic) screened ladder approximation.[6,7] In this formalism, the many-body effects of the plasma on absorption are the screening of the Coulomb enhancement, phase-space filling (PSF) by the carriers, and band gap renormalization (BGR). These effects can be viewed as density-dependent optical nonlinearities caused by the quasiequilibrium plasma.[3,4] A two-band model is used for the conduction and valence bands by either ignoring the light hole (*lh*) band or lumping it with the heavy hole (*hh*) band via an effective valence band density of states.[8]

Photoexcited carriers may be spin polarized by the optical orientation technique.[9] It is based on the selection rules for transitions induced by circularly polarized light from both *hh* and *lh* bands into the conduction band. A three-band SBE to model intervalence band coherence of quantum wells, under circularly polarized photoexcitation, was formulated,[10] which included *hh*-*lh* band coupling. For modeling optical response in carrier spin-polarized bulk and quantum well semiconductors, a very general six-band SBE has been recently framed and applied (after neglecting some terms) to give a microscopic description of spin dynamics.[11–13] As was done for the (spin-unpolarized) semiconductor laser,[4] it maybe desirable to solve such model, spin-SBEs, in the quasiequilibrium regime, for a microscopic understanding of a new type of spin optoelectronic device, the spin vertical cavity surface emitting laser (spin VCSEL).[14]

In the quasiequilibrium regime, using the pump-probe technique, Nemec *et al.*[15] recently studied absorption spectra in carrier spin-polarized bulk GaAs at room temperature. They observed a spectral crossover in the difference in absorption between right (σ^+) and left (σ^-) circularly polarized lights. This circular dichroism experienced by the probe is due to the electronic spin polarization excited by an earlier σ^+ pump pulse. For a microscopic description of this experiment, we present the spin-modified solution of the Bethe-Salpeter equation, extended to include the *lh* band. Our approach is equivalent to solving the full spin-SBEs in the quasiequilibrium regime, but neglecting the terms corresponding to *hh*-*lh* coupling, spin splitting of the single particle states, and electron-hole exchange interaction. The last two terms are important for spin relaxation processes, but not for optical transitions. *hh*-*lh* coupling was neglected because it is important only for intervalence band processes. Numerical simulations based on this framework showed the spectral crossover and were in reasonable agreement with the experimental spin-dependent, density-dependent, and spectral trends. The Bethe-Salpeter equation may therefore be useful in modeling spin-dependent many-body effects in semiconductors in the quasiequilibrium regime.

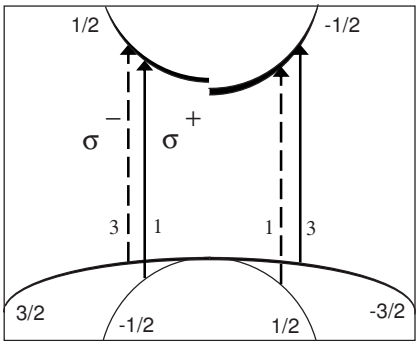

FIG. 1. Selection rules in schematic band structure of bulk GaAs at the center of the Brillouin zone, with $n_\downarrow > n_\uparrow$. Incident light is assumed to be propagating in the z direction. Bands are labeled with their m_J indices, where m_J is the component of total angular momentum J along z direction. Solid and dashed arrows, with the relative transition rates indicated at their base, correspond to σ^+ and σ^- helicities of the probe. $\downarrow$ and $\uparrow$ electron bands are labeled with $m_J=-1/2$ and $1/2$, respectively. The spin-unpolarized valence bands are labeled with $m_J=\pm 3/2$ (hh) and $\pm 1/2$ (lh). PSF at a nonzero temperature is shown by the gradation in thickness of the bands (the small PSF of the lh band has not been shown). The greater BGR of the $\downarrow$ band causes its band edge to be lower compared to the $\uparrow$ band.

II. METHOD

We first modify the solution of the Bethe-Salpeter equation for spin polarization (ξ) and inclusion of lh. Then, the method used to compare with the time-dependent experimental data[15] is described.

A. Spin-polarized optical susceptibility (including light holes)

At $t=0$, both electron and hole spins are created by the right circularly polarized pump pulse in the experiment; however, hole spins relax within $t \lesssim 100$ fs leaving behind a spin polarization only from electrons. The selection rules favor creating spin-down ($\downarrow$) electrons from the hh band three times as much as spin-up ($\uparrow$) electrons from the lh band ($\downarrow$ and $\uparrow$ electrons have their spin opposite and along the propagation direction of the pump, respectively). Moreover, the joint density-of-states effective mass for hh transitions $m_{r,hh}$ is nearly twice $m_{r,lh}$ for lh transitions. These two factors cause $n_\downarrow=6n_\uparrow$, as pointed out in Ref. 16 ($n_\downarrow+n_\uparrow=n$, the plasma density). So at $t=0$, the spin polarization $\xi_{\max}=5/7$, where ξ is defined as

$$\xi = \frac{n_\downarrow - n_\uparrow}{n_\downarrow + n_\uparrow}.$$

Later, the same selection rules involving the hh and lh bands determine the absorption of the right (σ^+) or left (σ^-) circularly polarized probes (Fig. 1). Therefore, here, the absorption depends not just on the total density of electrons and holes (as described in Refs. 3–8 for $\xi=0$) but individually on $n_\downarrow$, $n_\uparrow$, n_{hh}, and n_{lh}.

PSF reduces absorption since lesser number of states are made available for optical transitions. BGR increases absorption since the transitions take place at larger wave vector, as the band gap is narrowed. PSF and BGR, which are density dependent, are different for transitions into the $\downarrow$ and $\uparrow$ electron bands (Fig. 1). As will be seen later, these transitions also have a different Coulomb enhancement because the enhancement itself depends on PSF and BGR. All this affects the susceptibility $\chi^{cv}(\omega)$ pertaining to optical transitions from the valence ($v=hh,lh$) to the conduction ($c=\downarrow,\uparrow$) bands. The complex susceptibility $\chi^{\pm}(\omega)$ for $\sigma^{\pm}$ can be written as a sum of two such transitions (Fig. 1),

$$\chi^+(\omega) = \chi^{\downarrow,hh}(\omega) + \chi^{\uparrow,lh}(\omega), \tag{1a}$$

$$\chi^-(\omega) = \chi^{\uparrow,hh}(\omega) + \chi^{\downarrow,lh}(\omega). \tag{1b}$$

Here, χ^+ is sensitive to the $\downarrow$ band, whereas χ^- is weighted toward the $\uparrow$ band, because the transition from the hh band is favored over that from the lh band. Therefore, in general, a circular dichroism results from a nonzero ξ. The complex optical dielectric function $\epsilon^{\pm}(\omega)$ is obtained from $\chi^{\pm}(\omega)$ using

$$\epsilon^{\pm}(\omega) = \epsilon_\infty + 4\pi\chi^{\pm}(\omega), \tag{2}$$

from which the absorption $\alpha^{\pm}(\omega)$ and circular dichroism $\Delta\alpha(\omega)=\alpha^+(\omega)-\alpha^-(\omega)$ were obtained. Also, since linearly polarized light can be written in terms of σ^+ and σ^-, we obtain

$$\chi^0 = \frac{\chi^+ + \chi^-}{2}, \tag{3}$$

where χ^0 is the susceptibility of linearly polarized light. It may be verified that if $\xi=0$, $\chi^0=\chi^+=\chi^-$.

The complex optical susceptibility $\chi^{cv}(\omega)$ of a particular transition was related to the microscopic susceptibility $\chi^{cv}(k,\omega)$ by

$$\chi^{cv}(\omega) = \frac{1}{L^3}\sum_{\mathbf{k}} d^{cv}(k)\chi^{cv}(k,\omega). \tag{4}$$

The sum over wave vector does *not* include the spin degeneracy. The interband dipole matrix element for circularly polarized light $d^{cv}(k)$ reflected the selection rules,

$$d^{cv}(k) = \frac{e\hbar P_0}{m_0 E_g\left(1+\frac{\hbar^2k^2}{2m_{r,v}E_g}\right)} \quad (v=hh) \tag{5a}$$

$$= \sqrt{\frac{1}{3}}\frac{e\hbar P_0}{m_0 E_g\left(1+\frac{\hbar^2k^2}{2m_{r,v}E_g}\right)} \quad (v=lh), \tag{5b}$$

where m_0 is the free electron mass, $m_{r,v}=(1/m_e+1/m_v)^{-1}$, and E_g is the band gap. The momentum matrix element P_0, in an eight-band model,[17] is given by

$$P_0^2 \simeq \frac{m_0 E_g}{2}\left(\frac{m_0}{m_e}-1\right)\frac{3E_g+3\Delta_{so}}{3E_g+2\Delta_{so}}, \tag{6}$$

where Δ_{so} is the spin-orbit splitting of the valence band at the center of the Brillouin zone.

1. Interacting optical spectrum

We repeat the steps for obtaining $\chi^{cv}(\omega)$ outlined in Ref. 18, but with modifications for *lh* and spin. $\chi^{cv}(k,\omega)$, which causes the dichroism, is obtained by numerically solving the effective Bethe-Salpeter equation describing the repetitive electron-hole scattering (ladder approximation),

$$[\hbar\omega - E_g - \Delta E_g^{cv} + i\gamma^{cv}(k,\omega)]\chi^{cv}(k,\omega) = -[1 - f_c(k) - f_v(k)] \times \left[d^{cv}(k) + \sum_{\mathbf{k}'} V_s(|\mathbf{k}-\mathbf{k}'|)\chi^{cv}(k',\omega) \right]. \quad (7)$$

The screened Coulomb potential $V_s(q)$ derived in the random phase approximation and simplified in the quasistatic single plasmon-pole approximation is given by

$$V_s(q) = \frac{1}{L^3}\frac{4\pi e^2}{\epsilon_0 q^2}\left[1 - \frac{1}{1 + \frac{q^2}{\kappa^2} + \left(\frac{\nu_q}{\omega_{pl}}\right)^2}\right], \quad (8)$$

$$\omega_{pl}^2 = \frac{4\pi e^2}{\epsilon_0}\sum_j \frac{n_j}{m_j} \quad (j = \downarrow, \uparrow, hh, lh), \quad (9)$$

$$\kappa^2 = \frac{4\pi e^2}{\epsilon_0}\sum_j \frac{\partial n_j}{\partial \mu_j}, \quad (10)$$

where μ_j is the chemical potential, ω_{pl} and κ are the $3d$ plasma frequency and wave number, respectively, and ν_q^2 simulates the electron-pair continuum. Note that ω_{pl} and κ have been made ξ dependent. In Eq. (7), the factor $[1 - f_c(k) - f_v(k)]$ causes PSF. The Fermi functions $f_j(k)$ that described the distribution of the electrons and holes were

$$f_j(k) = \frac{1}{\exp\{\beta[E_j(k) - \mu_j]\} + 1}, \quad (11)$$

where $E_j(k) = \hbar^2 k^2/(2m_j)$ and $\beta = 1/(k_B T)$. We ignored the small spin dependence of the electron mass[19] (i.e., $m_\downarrow = m_\uparrow = m_e$). Besides, the nonparabolic or anisotropic nature of the bands, especially of the *hh*, has been neglected for the sake of simplicity. The BGR, ΔE_g^{cv}, for an optical transition between the valence band and the conduction band is

$$\Delta E_g^{cv}(k) = e_c(k) + e_v(k). \quad (12)$$

The self-energy $e_j(k)$ of the jth quasiparticle, in the quasistatic approximation, is

$$e_j(k) \simeq -\sum_{\mathbf{k}'} V_s(|\mathbf{k}-\mathbf{k}'|)f_j(k') + \frac{1}{2}[V_s(r=0) - V(r=0)], \quad (13)$$

where the first term is the "screened exchange" and the second term is the "Coulomb hole." The Coulomb-hole term is the same for each of the j quasiparticles. In Eq. (8), ν_q^2, which simulates the electron-pair continuum, as well as the temperature-dependent damping $\gamma^{cv}(k,\omega)$ and band gap E_g in Eq. (7) were obtained from Refs. 18 and 5. The chemical potentials μ_j, assuming that the electrons and holes were in quasiequilibrium, was obtained using a form of the Aguilera-Navarro approximation.[18] The *hh* and *lh* have the same chemical potential because they are in equilibrium with each other.

Rearranging Eq. (7), we obtained

$$\chi^{cv}(k,\omega) = \chi_0^{cv}(k,\omega)\left[1 + \frac{1}{d^{cv}(k)}\sum_{\mathbf{k}'} V_s(|\mathbf{k}-\mathbf{k}'|)\chi^{cv}(k',\omega)\right], \quad (14)$$

where

$$\chi_0^{cv}(k,\omega) = -\frac{d^{cv}(k)[1 - f_c(k) - f_v(k)]}{\hbar\omega - E_g - \Delta E_g^{cv} + i\gamma^{cv}(k,\omega)}. \quad (15)$$

To obtain the correct crossover between gain and absorption with $\gamma^{cv}(k,\omega)$, $\chi_0^{cv}(k,\omega)$ was described by a spectral representation.[18] By defining

$$\chi^{cv}(k,\omega) = \Gamma^{cv}(k,\omega)\chi_0^{cv}(k,\omega), \quad (16)$$

and substituting it into Eq. (14), we obtained for the vertex function $\Gamma^{cv}(k,\omega)$,

$$\Gamma^{cv}(k,\omega) = 1 + \frac{1}{d^{cv}(k)}\sum_{\mathbf{k}'} \bar{V}_s(k,k')\chi_0^{cv}(k',\omega)\Gamma^{cv}(k',\omega). \quad (17)$$

Here, $V_s(|\mathbf{k}-\mathbf{k}'|)$ has been replaced in Eq. (17) by its angle-averaged value $\bar{V}_s(k,k')$ because we assumed that only s-wave scattering contributed to the optical transitions. We used a matrix of approximately 200×200 Gauss-Legendre quadrature points to represent the vertex integral equation [Eq. (17)]. The diagonal singularity of the matrix was regularized by the compensation technique,[7] before it was inverted to give the solution for $\Gamma^{cv}(k,\omega)$. The complex optical susceptibility $\chi^{cv}(\omega)$ of a particular transition was obtained from

$$\chi^{cv}(\omega) = \frac{1}{L^3}\sum_{\mathbf{k}} d^{cv}(k)\Gamma^{cv}(k,\omega)\chi_0^{cv}(k,\omega), \quad (18)$$

where we substituted Eq. (16) in Eq. (4).

2. Noninteracting optical spectrum

If $\Gamma^{cv}(k,\omega)$ is neglected in Eq. (18), we obtain the "noninteracting" susceptibility, which differs from the truly noninteracting susceptibility due to the BGR term present in $\chi_0^{cv}(k,\omega)$ [cf. Eq. (15)]. $\Gamma^{cv}(k,\omega)$, which depends on PSF and BGR [cf. Eq. (17) and (15)], causes the excitonic resonances and the Coulomb enhancement. This is because $\Gamma^{cv}(k,\omega)$ expresses the influence of multiple electron-hole scattering (resulting from their attractive interaction) on the susceptibility.

It is difficult to separate PSF and BGR in the interacting $\Delta\alpha(\omega)$ due to the presence of the $\Gamma^{cv}(k,\omega)$ term. Therefore, we used the noninteracting $\chi^{cv}(\omega)$ to study how competition between PSF and BGR influences $\Delta\alpha(\omega)$.

In our calculated spectra, we took the spectral representation for only the imaginary part of $\chi_0^{cv}(k,\omega)$.[18] Also, the

k-dependent BGR was taken as a rigid shift at $k_F = (3\pi^2 n)^{1/3}$. These simplifications are not expected to significantly affect the results. The material parameters used were exciton Rydberg $E_0 = 4.2$ meV, exciton Bohr radius $a_0 = 125$ Å, electron mass $m_e = 0.0665 m_0$, *hh* mass $m_{hh} = 0.457 m_0$, *lh* mass $m_{lh} = 0.08 m_0$, $\Delta_{so} = 0.341$ eV $\epsilon_0 = 13.71$, $\epsilon_\infty = 10.9$, and $T = 295$ K.

B. Comparison with experiment

The probe spectral width was accounted for by adding its "half width at half maximum" value of 15 meV to $\gamma^{cv}(k,\omega)$ in the calculation. The experimental data are mostly in terms of the normalized differential transmittance D,

$$D = \frac{\left(\frac{\Delta T}{T}\right)^+ - \left(\frac{\Delta T}{T}\right)^-}{\left(\frac{\Delta T}{T}\right)^+ + \left(\frac{\Delta T}{T}\right)^-}. \tag{19}$$

Here, $(\Delta T/T)^\pm = (T^\pm - T)/T$, where $T^\pm$ is the transmission of probe $\sigma^\pm$ after the sample is pumped with σ^+. T is the unpumped transmission through the bulk sample of thickness $w \approx 1$ μm. If the change from the unpumped absorption $\Delta\alpha^\pm$ is such that $\Delta\alpha^\pm \ll 1/w \approx 10^4$ cm^{-1}, we can write D as

$$D \simeq \frac{\Delta\alpha^+ - \Delta\alpha^-}{\Delta\alpha^+ + \Delta\alpha^-} \tag{20a}$$

$$= \frac{\alpha^+ - \alpha^-}{\alpha^+ + \alpha^- - 2\alpha_0} = \frac{\Delta\alpha}{\alpha^+ + \alpha^- - 2\alpha_0}. \tag{20b}$$

The unpumped absorption $\alpha_0(\omega)$ could be calculated from $\chi^0(\omega)$ with $\xi = 0$ and the background doping density of the sample,[15] $n_0 = 10^{15}$ cm^{-3}. The sign of D is opposite to that of $\Delta\alpha$ because screening by the pumped carriers usually reduces the absorption, i.e., $\alpha^+ + \alpha^- - 2\alpha_0$ is a negative quantity. Furthermore, D is not affected by an overall density-independent scaling factor $C(\omega)$ that could multiply the calculated absorption, since D is a normalized quantity. Usually, $C(\omega)$ is needed to match the calculated absorption to the experimental value of absorption in a "pure," unexcited sample.[8]

The ξ-dependent calculations were compared with the time-dependent experimental data by using the following equation describing spin relaxation:

$$\xi(t) = \xi_{\max} e^{-2t/\tau_s}, \tag{21}$$

where $\xi_{\max} = 5/7$ and the spin relaxation time[15] $\tau_s = 130$ ps. We assumed a temporally constant plasma density n since $t \ll \tau_r \approx 1$ ns, where τ_r is the carrier recombination time.

III. RESULTS AND DISCUSSION

We show that our calculation captures all the trends in the experimental data in probed energy $h\nu$, spin polarization ξ, and pumped density n. To explain how PSF and BGR cause a (ξ-independent) crossover in $\Delta\alpha$, we first discuss the results for noninteracting $\Delta\alpha$. After showing the effect of the Coulomb interaction on $\Delta\alpha$, we finally compare the results for interacting $\Delta\alpha$ with the data. The agreement with the data comes directly from our calculation, without requiring us to adjust ξ, n, or sample-dependent broadening.

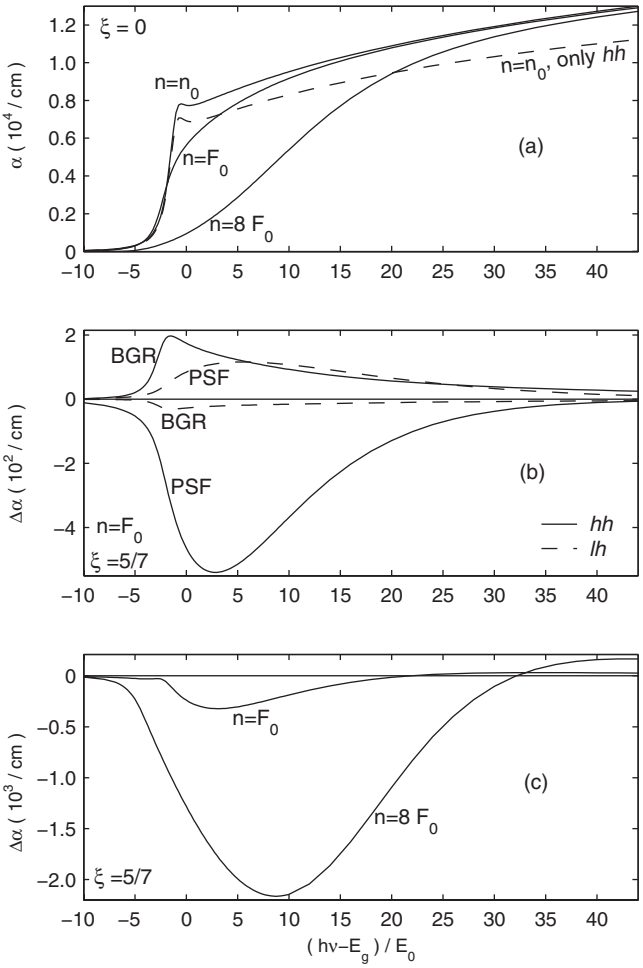

FIG. 2. (a) Spin-unpolarized interacting α, with background $n_0 = 10^{15}$ cm^{-3} and photoexcited plasma densities $F_0 = 1.3 \times 10^{17}$ cm^{-3} and $8F_0$. The dashed curve differs from the solid curve with $n = n_0$ by the neglect of *lh*. (b) Noninteracting $\Delta\alpha$ decomposed into *hh* and *lh* transitions, each of which has contributions from PSF and BGR. Within a transition, PSF and BGR oppose each other. Between transitions, PSF and BGR from *hh* oppose those from *lh*. (c) Density dependence of total noninteracting $\Delta\alpha$. The curve for $n = F_0$ can be obtained by summing together the curves in (b).

We did two checks on the spin-polarized calculation. Setting $\xi = 0$ gave back the unpolarized absorption [Fig. 2(a)], as calculated by Ref. 18, for different plasma densities. At lower densities, with $\xi = 0$, we also obtained the broadened Elliott's formula[20] by removing the k dependence of $\gamma^{cv}(k,\omega)$ and $d^{cv}(k)$. The discrepancy with Elliott's formula was $\approx 10^{-3}$ for photon energies that exceeded the band gap.

Inclusion of *lh* serves only to enhance the unpolarized absorption by 1/6, 1/3 from the matrix element, and 1/2 from the density of states [compare dashed and solid curves for $n = n_0$ in Fig. 2(a)]. Treating *lh* independently (without

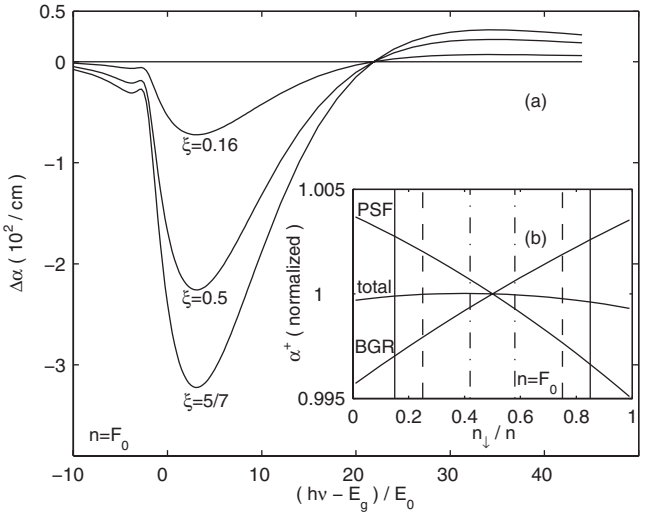

FIG. 3. (a) ξ dependence of noninteracting $\Delta\alpha$. (b) PSF and BGR components of noninteracting α^+ at the crossover energy vs $n_\downarrow$ (neglecting *lh* band). The ordinate is normalized to the value of α^+ at $n_\downarrow = n/2$, whereas the abscissa is normalized to n. The opposite $n_\downarrow$ dependence of PSF and BGR add up to give the total α^+ (scaled by 0.5) that is almost $n_\downarrow$ independent. The ξ independence of $\Delta\alpha$ at the crossover energy in (a) may be obtained from the difference of the value of total α^+ at the $n_\downarrow$ values shown by vertical solid lines ($\xi = 5/7$), dashed lines ($\xi = 0.5$), and dot-dashed lines ($\xi = 0.16$).

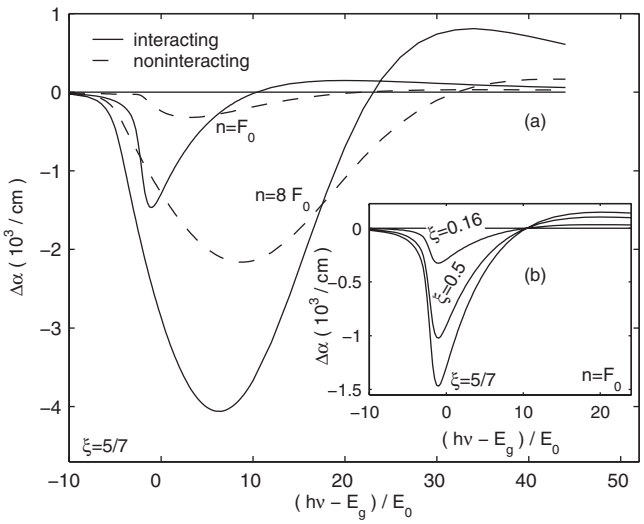

FIG. 4. (a) Density dependence of interacting $\Delta\alpha$. The corresponding noninteracting $\Delta\alpha$ shown is identical to Fig. 2(c). (b) ξ dependence of interacting $\Delta\alpha$.

hh-lh coupling) did not lead to noticeable artifacts in the calculated absorption.

A. Noninteracting optical spectra

The microscopic noninteracting calculation agrees with the earlier simplified explanation[15] that the $\Delta\alpha$ crossover is caused by competition between PSF and BGR. Within a transition (either *hh* or *lh*), PSF dominated at lower energies whereas BGR (of the opposite sign) dominated at higher energies. Moreover, PSF and BGR from *lh* transitions were opposite in sign [due to the selection rules in Eq. (1)] compared to those from *hh* transitions [Fig. 2(b)]. The $\Delta\alpha$ crossover shifted to higher energies as n was increased because PSF became more important[15] [Fig. 2(c)].

In contrast, the $\Delta\alpha$ crossover energy was independent of ξ, at a fixed n [Fig. 3(a)], due to the PSF and BGR interplays. A similar ξ-independent crossover occurred at higher energies, if *hh* transitions alone were considered. The weaker *lh* transitions did not result in a crossover in $\Delta\alpha$ in the energy interval shown, as can be verified by summing the dashed curves in Fig. 2(b). Since ξ determines $n_\downarrow$ relative to $n_\uparrow$, we study the cause of the ξ-independent crossover by plotting α^+ (inducing transitions only between the *hh* and $\downarrow$ bands after neglecting the *lh* transitions) vs $n_\downarrow$ [Fig. 3(b)]. Analogous results were obtained by plotting α^- vs $n_\uparrow$. The $n_\downarrow$ independence of total α^+ at the crossover energy, indicates that opposing trends between PSF and BGR for each helicity of light, caused the $\Delta\alpha$ crossover to be independent of ξ.

B. Interacting optical spectra

The Coulomb interaction increased the magnitude of $\Delta\alpha$ and shifted its crossover energy, but it did not affect the trends in $h\nu$, n, and ξ. The interaction caused a sharp peak near the band gap (due to excitonic effects) in the interacting $\Delta\alpha$, for $n = F_0$, and also enhanced it at higher energies compared to the noninteracting $\Delta\alpha$ [compare solid and dashed curves for $n = F_0$ in Fig. 4(a)]. At $n = 8F_0$, the peak near the band gap in the interacting $\Delta\alpha$ was not as pronounced (due to the almost complete excitonic ionization) compared to the noninteracting case [solid and dashed curves for $n = 8F_0$ in Fig. 4(a)]. However, at higher energies, they show a persisting Coulomb enhancement even at $n = 8F_0$. This is because the screening by the plasma is not very effective at high energies[8] (hence, the solid curves for $n = n_0$ and $8F_0$ in Fig. 2(a) approach each other at high energies). However, the ξ independence of the $\Delta\alpha$ crossover energy was preserved, despite Coulomb interactions [Fig. 4(b)]. We found that the pump-induced changes in the refractive index obtained from the complex susceptibility $\chi_0^{cv}(\omega)$ shifted the crossover by 3% to lower energy [for the solid curve $n = F_0$ in Fig. 4(a)]. The cause of the shift of the crossover to lower energies when we compare the interacting with the noninteracting curves is unclear.

C. Comparison with experiment

We compare our calculation with the experiment by accounting for probe width in the broadening [Fig. 5(a)]. We think that spectral averaging due to this additional broadening causes the crossover to shift from $(h\nu - E_g)/E_0 = 10.5$ [solid curve for $n = F_0$ in Fig. 4(a)] to $(h\nu - E_g)/E_0 = 15.3$. Because D is plotted instead of $\Delta\alpha$ in Fig. 5(a), there is an overall flip of sign compared to Fig. 4.

Our model reproduces the experimental observations that D changes sign either as λ is varied at a fixed n [Fig. 5(a)] or n is varied at a fixed λ [Fig. 5(b)]. Furthermore, the expected ξ independence of the crossover energy [Fig. 4(b)] is indeed shown by the data (flat dashed curve in Fig. 6). The tendency of D to change sign at a fixed probe wavelength or energy

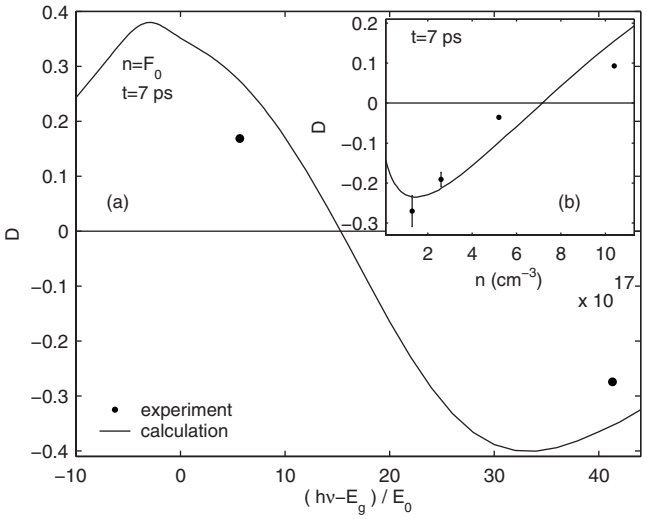

FIG. 5. Comparison with experiment. (a) Spectral D. The data points are obtained from Figs. 4(b) and 6(b) of Ref. 15 at $t=7$ ps. (b) Density dependence of D at a fixed probe energy. The experimental points are for $n=F_0$, $2F_0$, $4F_0$, and $8F_0$, again at $t=7$ ps [from Fig. 7 of Ref. 15]. The calculation used $\lambda=816$ nm, whereas experimentally, $\lambda=775$ nm. Vertical bars indicate the experimental noise.

[Fig. 5(b)] as n is increased occurred over a certain range of energies. This tendency is also shown by $\Delta\alpha$ over $10.5 < (h\nu - E_g)/E_0 < 23.1$ [solid curves for $n=F_0$ and $8F_0$ in Fig. 4(a)]. Outside this range $|D|$ increased, without flipping its sign, with n. We cannot obtain the carrier thermalization part of the experimental spectra ($t<1$ ps) in Fig. 6 because it has not been accounted for in the calculation.

The maximum value of D due to PSF is 0.35 (instead of 0.25 as stated in Ref. 15). This is because, by assuming $\Delta\alpha \sim -n$ in Eq. (20a), we obtain $D=\xi/2$ and as noted in Sec. II, $\xi_{\max}=5/7$. The numerically calculated D supported the above reasoning: in Figs. 5 and 6, $D \lesssim 0.35$ at lower energies. However, near the band gap, perhaps the excitonic nonlinearity slightly increased the value of D [Fig. 5(a)]. The calculated $|D|$ exceeds 0.35 also at higher energies where PSF is expected to be less important (since D is negative).

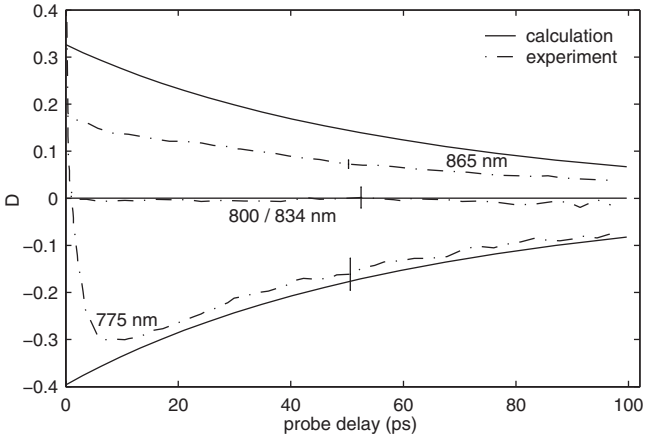

FIG. 6. Comparison with experiment (dot-dashed lines) regarding evolution of D at the probe $\lambda=775$, 800 (834 nm in the calculation), and 865 nm. The experimental data are obtained from Fig. 8 of Ref. 15. Pumped densities are 1.3×10^{17}, 6×10^{16}, and 2×10^{16} cm^{-3} respectively (Ref. 15). Vertical bars indicate the experimental noise.

In Figs. 5(b) and 6, for trends near the crossover energy, the calculation used $\lambda=816$ nm and $\lambda=834$ nm instead of the actual probes $\lambda=775$ nm and $\lambda=800$ nm, respectively. This mismatch in the crossover energy could be due to several reasons. The quasistatic approximation used here is justified for the *hh* band due to its large mass, but it is known to be unsatisfactory for the conduction band.[8] A better result is expected by using dynamic screening instead. We have shown that n [compare $n=F_0$ and $n=8F_0$ curves in Fig. 4(a)] and broadening (as indicated earlier in this section) strongly influence the crossover energy. Experimental uncertainties in the photoexcited carrier density n (by a factor of 2) and the sample-dependent broadening (taken equal to the probe width), neither of which were adjusted for, would have shifted the crossover to higher energies by 22% and 77%, respectively. However, we stress that although in Figs. 5(b) and 6 the calculation does not yield the experimental crossover energy, the fact that it captures the trends in $h\nu$, ξ, and n shown by the data suggests that we have incorporated the relevant physics. Studying the effect of *hh* anisotropy on the results,[21] we found that the crossover shifted to lower energies by 13% for $m_{hh}=0.91m_0$ (along the L direction) and to higher energies by 10% for $m_{hh}=0.35m_0$ (along the X direction) for the $n=F_0$ curve in Fig. 4(a). We also tried to adjust within a factor of 2 the values of ν_q^2 and the numerical constant α [describing $\gamma(k,\omega)$],[18] but found that the crossover energy changed by $\lesssim 1\%$.

IV. CONCLUSION

We have provided a method to calculate spin-polarized many-body effects in the room temperature absorption spectra of bulk GaAs. This was done by modifying the existing microscopic theory for absorption, which is known to match experiment over a wide range of plasma densities. Light hole contributions were also included. The agreement with results of a recent circularly polarized pump-probe experiment came directly from our calculation, without requiring us to adjust spin-polarization, plasma density, or sample-dependent broadening. We find that the $\Delta\alpha$ crossover and the experimental spin-dependent, density-dependent, and spectral features are reproduced, thus validating the use of our model to understand circularly polarized pump-probe experiments in III-V semiconductors, in the quasiequilibrium regime. This also opens up the possibility that the Bethe-Salpeter equation may be used to theoretically describe spin-dependent many-body nonlinearities in the operation of the spin VCSEL and perhaps make predictions about its performance.

ACKNOWLEDGMENT

We thank the Department of Science and Technology, Government of India, for partial financial support.

*arjun@physics.iisc.ernet.in

[1] I. Žutić, J. Fabian, and S. D. Sarma, Rev. Mod. Phys. **76**, 323 (2004).
[2] D. D. Awschalom and N. Samarth, in *Semiconductor Spintronics and Quantum Computation*, edited by D. D. Awschalom, D. Loss, and N. Samarth (Springer-Verlag, Germany, 2002).
[3] H. Haug and S. W. Koch, *Quantum Theory of the Optical and Electronic Properties of Semiconductors*, 3rd ed. (World Scientific, Singapore, 1990).
[4] H. Haug and S. W. Koch, Phys. Rev. A **39**, 1887 (1989).
[5] J. P. Löwenau, F. M. Reich, and E. Gornik, Phys. Rev. B **51**, 4159 (1995).
[6] J. P. Löwenau, S. Schmitt-Rink, and H. Haug, Phys. Rev. Lett. **49**, 1511 (1982).
[7] H. Haug and S. Schmitt-Rink, Prog. Quantum Electron. **9**, 3 (1984).
[8] R. Zimmermann, M. Rössler, and V. M. Asnin, Phys. Status Solidi B **107**, 579 (1981).
[9] M. I. Dyakonov and V. I. Perel, in *Optical Orientation*, edited by F. Meier and B. P. Zakharchenya (North-Holland, Amsterdam, 1984).
[10] R. Binder and M. Lindberg, Phys. Rev. B **61**, 2830 (2000).
[11] U. Rössler, Phys. Status Solidi B **234**, 385 (2002).
[12] C. Lechner and U. Rössler, Phys. Rev. B **72**, 045311 (2005).
[13] C. Lechner and U. Rössler, Phys. Rev. B **72**, 153317 (2005).
[14] J. Rudolph, D. Hägele, H. M. Gibbs, G. Khitrova, and M. Oestreich, Appl. Phys. Lett. **82**, 4516 (2003).
[15] P. Nemec, Y. Kerachian, H. M. van Driel, and A. L. Smirl, Phys. Rev. B **72**, 245202 (2005).
[16] M. Beck, Ph.D. thesis, Friedrich-Alexander-Universität, 2005.
[17] S. Datta, *Quantum Phenomena*, Modular Series on Solid State Devices (Addison-Wesley, Reading, 1989).
[18] C. Ell, R. Blank, S. Benner, and H. Haug, J. Opt. Soc. Am. B **6**, 2006 (1989).
[19] Y. Zhang and S. Das Sarma, Phys. Rev. Lett. **95**, 256603 (2005).
[20] A. R. Goñi, A. Cantarero, K. Syassen, and M. Cardona, Phys. Rev. B **41**, 10111 (1990).
[21] P. Langot, R. Tommasi, and F. Vallée, Phys. Rev. B **54**, 1775 (1996).